metals

MDPI

*Article*

# The Nucleation and the Intrinsic Microstructure Evolution of Martensite from $\{332\}\langle 113\rangle_\beta$ Twin Boundary in β Titanium: First-Principles Calculations

**Qiu-Jie Chen [1,2], Shang-Yi Ma [1,*] and Shao-Qing Wang [1]**

[1] Shenyang National Laboratory for Materials Science, Institute of Metal Research, Chinese Academy of Sciences, Shenyang 110016, China; qjchen16b@imr.ac.cn (Q.-J.C.); sqwang@imr.ac.cn (S.-Q.W.)

[2] School of Materials Science and Engineering, University of Science and Technology of China, Shenyang 110016, China

* Correspondence: shyma@imr.ac.cn

Received: 02 October 2019; Accepted: 04 November 2019; Published: 7 November 2019

**Abstract:** A clear understanding on the inter-evolution behaviors between $\{332\}\langle 113\rangle_\beta$ twinning and stress-induced martensite (SIM) $\alpha''$ in β-Ti alloys is vital for improving its strength and ductility concurrently. As the preliminary step to better understand these complex behaviors, the nucleation and the intrinsic microstructure evolution of martensite $\alpha''$ from $\{332\}\langle 113\rangle_\beta$ twin boundary (TB) were investigated in pure β-Ti at atomic scale using first-principles calculations in this work. We found the $\alpha''$ precipitation prefers to nucleate and grow at $\{332\}\langle 113\rangle_\beta$ TB, with the transformation of $\{332\}\langle 113\rangle_\beta$ TB→$\{130\}\langle \bar{3}10\rangle_{\alpha''}$ TB. During this process, $\alpha''$ precipitation firstly nucleates at $\{332\}\langle 113\rangle_\beta$ TB and, subsequently, it grows inwards toward the grain interiors. This easy transition may stem from the strong crystallographic correspondence between $\{332\}\langle 113\rangle_\beta$ and $\{130\}\langle \bar{3}10\rangle_{\alpha''}$ TBs, and the region close to the $\{332\}\langle 113\rangle_\beta$ TB presents the characteristics of intermediate structure between β and $\alpha''$ phases. Kinetics calculations indicate the $\alpha''$ phase barrierlessly nucleates at $\{332\}\langle 113\rangle_\beta$ TB rather than in grain interior, where there is higher critical driving energy. Our calculations provide a unique perspective on the "intrinsic" microstructure evolution of martensite $\alpha''$ from $\{332\}\langle 113\rangle_\beta$ TB, which may deepen our understanding on the precipitation of martensite $\alpha''$ and the inter-evolution behaviors between $\{332\}\langle 113\rangle_\beta$ twinning and martensite $\alpha''$ in β-Ti alloys at atomic scale.

**Keywords:** martensite phase transformation; phase transformation kinetics; titanium; first-principle calculation; twin boundary

## 1. Introduction

Metastable β-Ti alloys have some excellent properties, such as high strength, low density, and biocompatibility, which make them a promising material in aerospace and biomedical applications [1,2]. However, the lack of strain-hardening limits their use in advanced applications [3,4]. By controlling the stability of the β matrix through its chemical compositions, a strategy that triggers martensitic transformation and/or twinning under applied stress, termed transformation-induced plasticity (TRIP) and twinning-induced plasticity (TWIP), in β-Ti alloys has been developed to improve the strength and ductility concurrently [5–9]. It has been reported that the $\alpha''$ and ω phases, $\{332\}\langle 113\rangle_\beta$ and $\{112\}\langle 111\rangle_\beta$ twins are the major deformation products during the process of TRIP/TWIP, which are clearly observed in a variety of β-Ti alloys [10–12]. Generally, $\alpha''$ phases and

$\{332\}\langle 113\rangle_\beta$ twins are observed in a much larger volume fraction when the concentration of β-stabilizing element is low [13–16].

Sun et al. suggested that $\{332\}\langle 113\rangle_\beta$ twinning and stress-induced martensite (SIM) $\alpha''$ can be activated simultaneously from the onset of plasticity in a deformed Ti-12Mo (wt.%) alloy [13]. The volume fraction of both $\{332\}\langle 113\rangle_\beta$ twin boundary (TB) and SIM $\alpha''$ increases with strain. They further observed the activation of secondary $\{332\}\langle 113\rangle_\beta$ twinning and secondary $\alpha''$ precipitation within the primary $\{332\}\langle 113\rangle_\beta$ TB. The identical phenomenon was also noted in the very recent study of Ti–10V–4Cr–1Al (wt.%) by Lilensten et al. [15]. However, Castany et al. suggested that the $\{332\}\langle 113\rangle_\beta$ TB is not formed directly in the β phase, but is the result of the reversion of $\{130\}\langle \bar{3}10\rangle_{\alpha''}$ parent twins occurring in SIM $\alpha''$ phase under stress [14]. In their study of Ti–27Nb (at.%) alloy, the β phase transforms firstly into $\alpha''$ martensite which subsequently occurs $\{130\}\langle \bar{3}10\rangle_{\alpha''}$ twinning with increasing the applied strain; the $\alpha''$ martensite transforms back to the β phase, thereby leading to the transformation of $\{130\}\langle \bar{3}10\rangle_{\alpha''}$ to $\{332\}\langle 113\rangle_\beta$ TB when the stress is released [14]. The similar $\{332\}\langle 113\rangle_\beta$ twinning assisted by SIM $\alpha''$ was also observed in other Ti–Nb-based alloys [17,18]. It is seen that the formation and activation sequences of $\{332\}\langle 113\rangle_\beta$ TB and SIM $\alpha''$ in Ti–Mo (V) and Ti–Nb alloys during TRIP/TWIP processes are very different, or even in contrast. In the minds of Castany et al., $\{332\}\langle 113\rangle_\beta$ twinning is always formed from the reversion of $\{130\}\langle \bar{3}10\rangle_{\alpha''}$ twins in superelastic alloys due to its less stability, and the SIM transformation of $\{130\}\langle \bar{3}10\rangle_{\alpha''}$ twins still occurs but not in a reversible manner and leads to a TRIP effect when the β stability increases, and there is no more SIM transformation to initiate $\{332\}\langle 113\rangle_\beta$ twinning in more stable β phase, making the classical $\{112\}\langle 111\rangle_\beta$ twinning easier to form instead [14]. As a better β-stabilizer of Mo than Nb [19,20], it is expected that SIM $\alpha''$ is more difficult to be formed in Ti–Mo than in Ti–Nb. However, it is the fact that SIM $\alpha''$ was activated at the strain of 0.7% in Ti–12Mo (wt.%) alloy [13], while the SIM $\alpha''$ was only found from 3% strain in Ti–27Nb (at.%) alloy which is superelastic [14].

It is seen that it is hard to reach a "universal mechanism" for the deformation product of $\{332\}\langle 113\rangle_\beta$ TB and SIM $\alpha''$ in β-Ti alloys, since the stability of β-Ti alloys is highly associated with the chemical compositions. The kind and concentration of the chemical elements largely dominate the specific mechanism of the deformation product of $\{332\}\langle 113\rangle_\beta$ TB and SIM $\alpha''$, and their activation sequence or inter-evolution behaviors. However, it is difficult to quantitatively reveal which and how the chemical elements control the formation behaviors of $\{332\}\langle 113\rangle_\beta$ TB and SIM $\alpha''$. As a preliminary step to better understand the complicated process of TRIP/TWIP, it is very important to uncover the "intrinsic" inter-evolution behaviors between $\{332\}\langle 113\rangle_\beta$ TB and SIM $\alpha''$, which is generally veiled by the complex effects of chemical compositions and external applied stress. In this work, we aim to unveil the "intrinsic" inter-evolution behaviors between $\{332\}\langle 113\rangle_\beta$ TB and SIM $\alpha''$ using a pure Ti model, which was chosen to eliminate the effects of chemical compositions, and to strive to describe the specific microstructure evolution from $\{332\}\langle 113\rangle_\beta$ TB using the first-principles method. Though this work is strongly limited to pure Ti and the external applied stress is not considered, a unique perspective on the microstructure evolution of $\{332\}\langle 113\rangle_\beta$ TB is provided at atomic scale, which is beyond the present experimental techniques.

## 2. Computational Methods and Model

### *2.1. Computational Methods*

Our first-principles calculations were performed with the density functional theory (DFT), as implemented in the VASP code [21–23]. The electron exchange–correlation interactions were described with the generalized gradient approximation of Perdew, Burke, and Ernzerhof (PBE) [24], and ion–electron interactions were treated with the projector-augmented wave (PAW) method [25], together with the plane wave basis set with a kinetic energy cutoff of 350 eV. During our calculations, all the degrees of atomic freedom (ions, cell volume, and shape) were relaxed using the conjugate gradient algorithm, with the convergence criteria for energy and force being $10^{-6}$ eV atom$^{-1}$ and 0.01 eV Å$^{-1}$, respectively. The results obtained with the conjugate gradient algorithm were further

examined and confirmed with the quasi-Newton algorithm and the generalized solid-state nudged elastic band (G-SSNEB) method [26] using similar convergence criteria.

### 2.2. $\{332\}\langle 113\rangle_\beta$ *Twin Boundary Model*

A grain boundary structure can be described as a combination of structural units in two dimensions [27]. Thus, the $\{332\}\langle 113\rangle_\beta$ TB model was constructed using the structural unit model [28,29] in our calculations, and the corresponding structural units were denoted with '*A*' (2-atom structural unit, blue region) and '*C*' (4-atom structural unit, green region) in Figure 1a,b. Note that the '*A*' unit simply describes the lattice of bcc crystal along $[0\bar{2}3]$ direction projected on $(1\bar{1}0)$ plane, and the '*C*' unit describes a tetrahedron projected on $(1\bar{1}0)$ plane. Our $\{332\}\langle 113\rangle_\beta$ TB model is consistent with the model used in other literatures [30,31]. The three lattice vectors of the bi-crystal model, $\{332\}\langle 113\rangle_\beta$ TB, $[1\bar{1}0]_\beta$, $[11\bar{3}]_\beta$, and $[332]_\beta$, were orientated in parallel with the *x*, *y*, and *z* axis, respectively, and periodic boundary conditions were applied in the three directions. The dimensions of the bi-crystal model were 4.59 × 5.39 × 50.66 Å, as listed in Table 1, with the *Γ*-centered Monkhorst-Pack [32,33] *k*-points grid of 11 × 9 × 1 used in the calculations. As shown in Figure 1a, the bi-crystal model adopted a "sandwich" configuration containing two identical $\{332\}\langle 113\rangle_\beta$ TBs positioned at the middle and the boundary of the model. In this case, the periodical TBs were separated by 34 atom planes in $[332]_\beta$ direction, with the distance about 25 Å. This distance was within the reasonable range between two TBs, which ensured the convergence of interfacial energy in other studies of TB in *α*-Ti [34,35]. Our tests also show that this distance can afford the convergent interface energy within the error of ~5 mJ/m$^2$. Thus, the interactions between the two TBs could be ignored and the final result was converged at such large distance in our work.

It is well known that pure β-Ti is unstable at 0 K under ambient pressure [36]. Therefore, the bi-crystal model containing $\{332\}\langle 113\rangle_\beta$ TB prefers to relax into the configuration with the lower energy directly, and the initial and optimal $\{332\}\langle 113\rangle_\beta$ TB cannot be obtained by direct relaxation. To eliminate any artificial influences during the modeling process as much as possible, the constructed $\{332\}\langle 113\rangle_\beta$ TB structure was optimized using static calculation method with the same convergence criteria mentioned above before full relaxation. Firstly, the interatomic distance $d_A$ between the atom '*0a*' and '*0b*' was changed by moving the atom '*0b*' along *y* axis, as shown in Figure 1b. The total energy is functioned with $d_A$, and it is minimum when $d_A$ = 1.87 Å, as the black line shown in Figure 1c. Thus, the optimal interatomic distance $d_A$ was 1.87 Å. Secondly, the $\{332\}\langle 113\rangle_\beta$ TB structure was further optimized by changing the interplanar spacing between the TB plane and its first neighboring atom plane with the interval of $\delta$ = 0.05 Å when $d_A$ was set to 1.87 Å. This optimization was applied on both sides of the TB simultaneously, $d_1 = d_{-1} = 2d + \delta$, where *d* is the interplanar spacing of (332) plane in bulk. The total energy as a function of $\delta$ is also illustrated in Figure 1c. As indicated by the blue line, the total energy is minimum when $\delta$ = −0.15 Å. Correspondingly, the optimal interplanar spacing is $d_1 = d_{-1}$ = 1.24 Å. Then, the optimized structure of $\{332\}\langle 113\rangle_\beta$ TB was used in following calculations.

In our calculations, the interface energy of interface *P*1/*P*2 for the two phases *P*1 and *P*2 was calculated as the following equation:

$$\gamma_{IT} = \frac{E_{total} - nE_{P1} - mE_{P2}}{S}, \quad (1)$$

where $E_{total}$ is the total energy of the supercell model containing interface *P1/P2*, *n* and *m* are the atom numbers of the phase *P*1 and *P*2 in the model, $E_{P1}$ and $E_{P2}$ are the energy per atom of the phase *P*1 and *P*2 in bulk state, respectively, and *S* is the interface area. For the calculation of TB, Equation (1) becomes as follows, since it consists of two same phases:

$$\gamma_{TB} = \frac{E_{total} - nE_P}{2S}, \quad (2)$$

where the factor 2 accounts for the two identical TBs in the model.

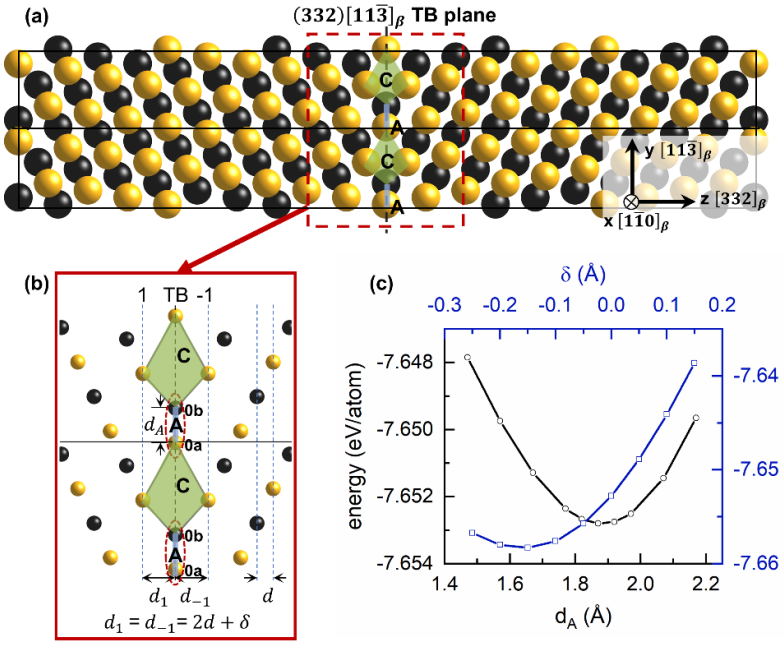


**Figure 1.** (**a**,**b**) The 1 × 2 × 1 initial configuration of $\{332\}\langle 113\rangle_\beta$ twin boundary (TB) projected on $(1\bar{1}0)$ plane. Yellow and black spheres represent the atoms at the adjacent $(1\bar{1}0)$ planes. Black dashed line denotes grain boundary plane, d is the interplanar spacing of (332) plane in bulk. '1' and '−1' denote the atomic planes. (**c**) The energy of the bi-crystal model as a function of $d_A$ and $\delta$.

**Table 1.** The lattice parameters of various interface models used in this work and the corresponding interface energies.

| Interfaces | Lattice Parameters (Å) | | | Interface Energy (mJ/m²) |
|---|---|---|---|---|
| | a | b | c | |
| $\{332\}\langle 113\rangle_\beta$ | 4.59 | 5.39 | 50.66 | 777.38 |
| $\{130\}\langle \bar{3}10\rangle_{\alpha''}$ | 4.59 | 10.62 | 37.45 | 76.71 |
| $(110)_\beta//(001)_{\alpha''}$ | 3.15 | 4.59 | 37.93 | 740.04 |

## 3. Results and Discussions

### *3.1. The Intrinsic Evolution from* $\{332\}\langle 113\rangle_\beta$ *TB to α Phase*

It should be noted that pure β-Ti is statically metastable (or dynamically unstable) in DFT simulation at 0 K [37,38]. Therefore, it sounds illogical to study the microstructure evolution of $\{332\}\langle 113\rangle_\beta$ TB in pure β-Ti from the black side view when the issue is divided into two sides. However, from the white side view, its static metastability indicates that β-Ti can naturally evolve into lower energy state along the gradient route of energy landscape once slight perturbation is introduced. Therefore, its static metastability can help us uncover the "intrinsic" microstructure evolution of $\{332\}\langle 113\rangle_\beta$ TB at atomic scale when it is introduced. As shown in Figure 2, it can be found that the initial β phase containing $\{332\}\langle 113\rangle_\beta$ TB (Figure 2a) experiences significant changes in structure, and finally relaxes into $\alpha$ phase (Figure 2e). There is no interface in the final relaxed structure. The lattice parameters of the relaxed unit-cell are $a$ = 2.93 Å and $c$ = 4.65 Å, which is in agreement with the measurements of hcp $\alpha$ phase [39], as listed in Table 2. Furthermore, the relaxed structure was further analyzed using radial distribution function $g(r)$, as illustrated in Figure 3. It can be found that the $g(r)$ of the relaxed structure is well consistent with that of the ideal $\alpha$ phase. It demonstrates that the final relaxed structure shown in Figure 2e is identical to the ideal $\alpha$ phase. Though it is thermodynamically expected that the metastable β-Ti prefers to relax into the stable $\alpha$

phase when any slightly perturbation is introduced, the evolution from $\{332\}\langle 113\rangle_\beta$ TB to the flawless $\alpha$ phase in our calculations implies the probability of $\alpha$ precipitation at $\{332\}\langle 113\rangle_\beta$ TB in β-Ti.

**Table 2.** The lattice parameters and energies of various Ti phases.

| Phases | Lattice Parameters (Å) | | | Energy (eV/atom) |
|---|---|---|---|---|
| | a | b | c | |
| β | 3.25 | | | −7.69 |
| | 3.32 [2] | | | |
| $\alpha''$ | 3.08 | 4.60 | 4.85 | −7.78 |
| | 2.94 [40] | 4.63 [40] | 5.01 [40] | |
| $\alpha$ | 2.93 | | 4.65 | −7.80 |
| | 2.96 [39] | | 4.69 [39] | |

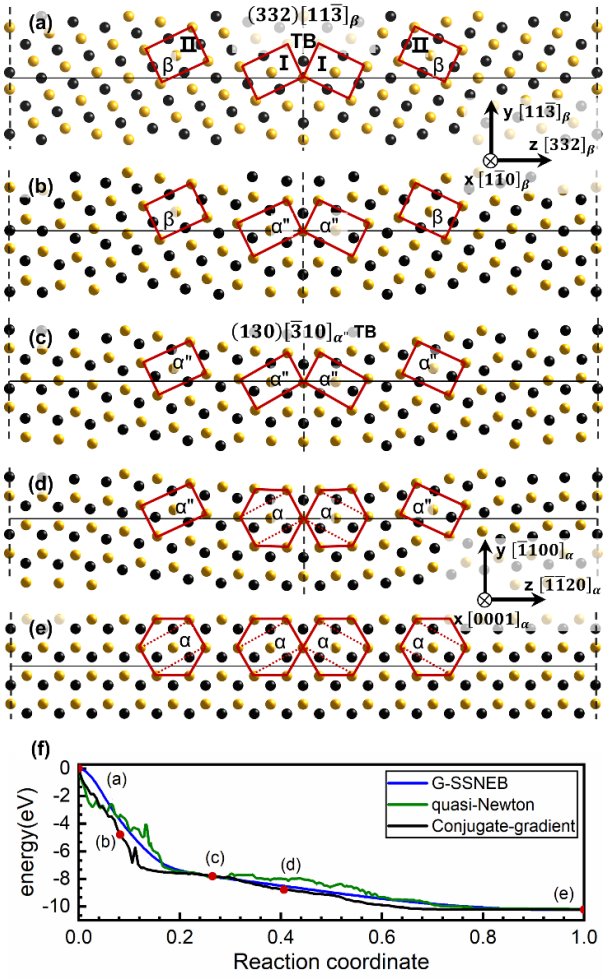


**Figure 2.** The intrinsic microstructure evolution of martensite ($\alpha''$ and $\alpha$) from $\{332\}\langle 113\rangle_\beta$ TB through the initial (**a**), intermediate (**b**–**d**), and the final (**e**) atomic configurations. The energy profiles obtained by the algorithms of the conjugate gradient, quasi-Newton, and G-SSNEB are shown in (**f**) for comparison. Yellow and black spheres represent the atoms in the adjacent $(1\bar{1}0)_\beta$ and $(0001)_\alpha$ planes, respectively. The unit-cells are outlined by the red lines.

To clearly show the microstructure evolution during this transformation, we analyzed the relaxation processes and determined a series of intermediate transition configurations representing the transformation sequence, as shown in Figure 2b–d. With the assistance of unit-cell *I* and *II* outlined by the red lines in Figure 2a, these transition configurations can provide the local structure

changes in details, especially for the displacement sequence of atoms in different regions, close to and far away from $\{332\}\langle 113\rangle_\beta$ TB. In comparison with the initial structure, one can observe the noticeable atoms displacements in the vicinity of $\{332\}\langle 113\rangle_\beta$ TB, which leads to the visible changes of unit-cell *I*, as shown in Figure 2b. The changed unit-cell *I* presents the characteristic of $\alpha''$ phase, which is base-centered orthorhombic (Cmcm) structure with atomic positions of (0, 0, 0), (1/2, 1/2, 0), (0, $y$, 0), and (0, 1/2+$y$, 1/2) in the unit-cell. The basal shuffle, $y$, changes with the different alloying element and composition [41]. In our work, the lattice parameters of $\alpha''$ phase are $a$ = 3.08 Å, $b$ = 4.60 Å, $c$ = 4.85 Å, and $y$ = 0.13 in Wyckoff position, which is in agreement with the measurements of $\alpha''$ phase, as listed in Table 2. It should be noted that $\alpha''$ phase is unstable in pure Ti. The $\alpha''$ phase here is just a snapshot of transition structure presenting the characteristic of $\alpha''$ phase to show the important intermediate transition state during the relaxation process. Additionally, the unchanged unit-cell *II* indicates that the atoms far away from the TB remain immobile at the same time. This suggests that the transformation firstly takes place at both sides of the $\{332\}\langle 113\rangle_\beta$ TB, resulting in the formation of $\alpha''$ embryos. As the continuation of this transformation, the $\alpha''$ embryos grow inwards toward the grain interiors, and then the grains transform from β into $\alpha''$ phase, and finally result in the formation of $(130)[\bar{3}10]_{\alpha''}$ TB, as shown in Figure 2c. Subsequently, the $\alpha$ embryos form at both sides of the $(130)[\bar{3}10]_{\alpha''}$ TB, as shown in Figure 2d, whereas the $\alpha''$ phase in grain interiors has yet to undergo transformation. As the transformation proceeding, the $\alpha$ embryos spread toward the grain interiors. Finally, the $(130)[\bar{3}10]_{\alpha''}$ TB disappears, and the β phase containing $\{332\}\langle 113\rangle_\beta$ TB completely transforms into $\alpha$ phase, as shown in Figure 2e. In addition, the abovementioned microstructure evolution was further examined and confirmed using the quasi-Newton algorithm and the G-SSNEB method. The identical microstructure evolution can also be observed in the calculations performed with the quasi-Newton algorithm and the G-SSNEB method. The energy profiles obtained by the conjugate gradient algorithm, quasi-Newton algorithm, and the G-SSNEB method are very similar, as shown in Figure 2f. This indicates that this microstructure evolution described by the conjugate gradient algorithm is reliable.

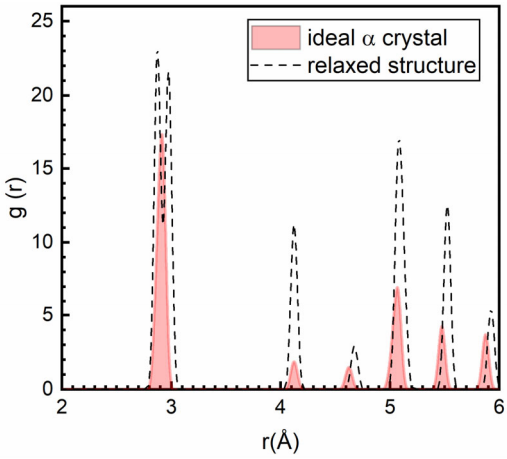


**Figure 3.** The radial distribution functions of ideal $\alpha$ crystal and the final relaxed structure.

### *3.2. The Different Displacements of Atoms Close to and Far Away from* $\{332\}\langle 113\rangle_\beta$ *TB*

Actually, the local microstructure evolutions at the TB and grain interior are somewhat different, which results in a different formation process of $\alpha$ phase at TB and in grain interior. To explicitly elaborate this difference, we tracked the atoms displacements in unit-cell *I* and *II*, and illustrated them in Figure 4. As shown in Figure 4a, the formation process of $\alpha$ phase at $\{332\}\langle 113\rangle_\beta$ TB involves two steps: The atoms (blue circle) initially go through shuffle to the sites of green circles, forming $\alpha''$ phase; subsequently, the atoms shift from green circles to orange ones, forming $\alpha$ phase. During this process, the shifts of atoms 1, 3, 5, and 7 to atoms 1″, 3″, 5″, and 7″ result in the contraction and expansion of lattices along $[001]_\beta$ and $[\bar{1}\bar{1}0]_\beta$ directions, respectively.

Different from the formation of $\alpha$ phase at $\{332\}\langle 113\rangle_\beta$ TB, the changes of unit-cell *II* indicate that the formation process of $\alpha$ phase in grain interior can be divided into three steps, as shown in Figure 4b. The first two steps associated with the formation of $\alpha''$ phase: The initial atoms (blue circles) shift to the sites of lavender circles, driving the formation of distorted $\alpha''$ phase; the atoms (lavender circles) then move to the green ones, forming $\alpha''$ phase. Subsequently, the atoms (green circles) shift to the sites of orange circles, and the $\alpha''$ phase converts into $\alpha$ phase. During the entire transformation, the lattices of β phase (plotted by atoms 13, 15, 17, and 19) experiences contraction and expansion along $[001]_\beta$ and $[\bar{1}\bar{1}0]_\beta$ directions, respectively. Meanwhile, the atoms 12, 14, 16, and 18 go through shuffle to atoms 12″, 14″, 16″, and 18″, forming the final $\alpha$ phase. The orientation relationships of β and $\alpha''$ phases are $[1\bar{1}0]_\beta//[001]_{\alpha''}$, $[00\bar{1}]_\beta//[100]_{\alpha''}$, $[110]_\beta//[010]_{\alpha''}$, in agreement with other literature [42].

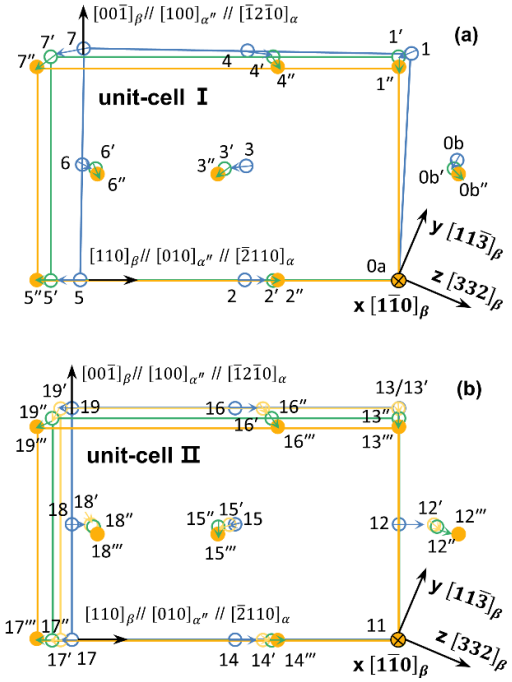


**Figure 4.** Schematic illustration of $\alpha$ phase formation process projected on the $(1\bar{1}0)_\beta$ plane at $\{332\}\langle 113\rangle_\beta$ TB (**a**) and grain interior (**b**), using the two unit-cell *I* and *II* shown in Figure 1a. Blue and orange circles denote the initial and final structures, respectively. Green and lavender circles denote the intermediate structures. All the atomic displacements refer to the original atom 0a (**a**) and 11 (**b**).

### *3.3. The Nucleation and Structure Evolution of Martensite from Crystallographic Perspective*

Our calculations uncover the intrinsic microstructure evolution of $\{332\}\langle 113\rangle_\beta$ TB to $\{130\}\langle\bar{3}10\rangle_{\alpha''}$ TB. This easy transition may stem from the strong crystallographic correspondence between $\{332\}\langle 113\rangle_\beta$ and $\{130\}\langle\bar{3}10\rangle_{\alpha''}$ TBs, as demonstrated by Bertrand et al. in the study of Ti–25Ta–20Nb alloys [43]. Under applied stress, the precipitation of $\alpha''$ martensite at $\{332\}\langle 113\rangle_\beta$ TB in β-Ti alloys has been observed in many experiments [13,15,44]. In our calculations, the complicated synergy effects of β-stabilizing elements and applied stress were fully eliminated. Thus, it is not reasonable to directly compare our results to these experiments. However, our calculations show that the nucleation and growth of $\alpha''$ precipitation at $\{332\}\langle 113\rangle_\beta$ TB is feasible. Based on this, it is reasonable to infer that the applied stress inducing the $\alpha''$ precipitation within $\{332\}\langle 113\rangle_\beta$ TB may partly play the role of facilitating the displacing of atoms to overcome the transition barrier of $\beta\rightarrow\alpha''$ at $\{332\}\langle 113\rangle_\beta$ TB in β-Ti alloys. Here, our calculations provide a unique perspective on the microstructure evolution and martensite precipitation at $\{332\}\langle 113\rangle_\beta$ TB, which can be used to better understand the experimental observed $\alpha''$ precipitation at $\{332\}\langle 113\rangle_\beta$ TB.

In our calculations, the formation of martensite is, in fact, induced by the higher interface energy of $\{332\}\langle 113\rangle_\beta$ TB, rather than applied stress, and driven by the energy difference between β and $\alpha''$ phases. As the calculated energies listed in Tables 1 and 2 (the interface energies were calculated using supercell model with lattice parameters listed in Table 1), the interface energy difference between $\{130\}\langle\bar{3}10\rangle_{\alpha''}$ and $\{332\}\langle 113\rangle_\beta$ TBs is about −700 mJ m$^{-2}$, and the energy difference between $\alpha''$ and β phases is about −0.09 eV atom$^{-1}$. Additionally, one can note that the $\alpha''$ phase can be formed by shifting the black atoms of β phase along the arrow collectively, as shown in Figure 5c. It is clearly seen that the displacements of black atoms in the vicinity of $\{332\}\langle 113\rangle_\beta$ TB are small compared with that in β phase. The radial distribution function (RDF) analysis further shows that $\{332\}\langle 113\rangle_\beta$ TB presents the structural characteristics between β and $\alpha''$ phases, as displayed in Figure 5d, which indicates that the unit-cell in the vicinity of $\{332\}\langle 113\rangle_\beta$ TB can be considered as an intermediate structure between β and $\alpha''$ phases. Therefore, the nucleation of $\alpha''$ phase at $\{332\}\langle 113\rangle_\beta$ TB is not only more favorable in energy, but also in crystallographic structure than its nucleation directly in β grain interior.

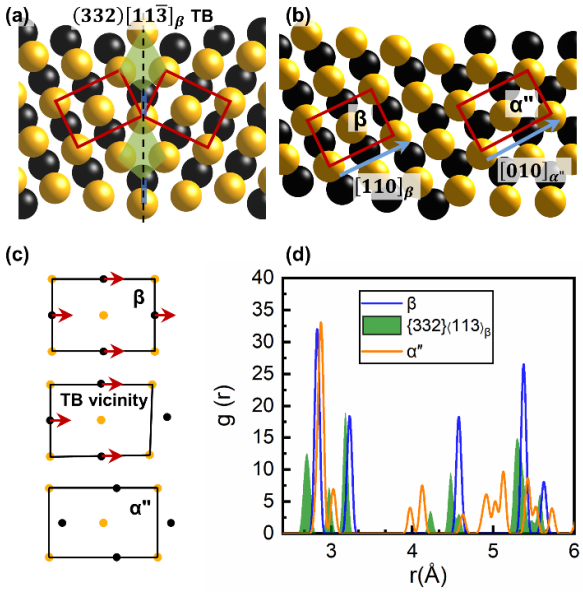


**Figure 5.** The illustration of $\alpha''$ formation through atom collective displacements. The local atomic configurations of $\{332\}\langle 113\rangle_\beta$ TB (**a**), β and $\alpha''$ (**b**). (**c**) The displacements of atoms projected on the $(1\bar{1}0)_\beta$ plane for the formation of $\alpha''$ phase in β phase and at $\{332\}\langle 113\rangle_\beta$ TB. (**d**) The radial distribution functions of β phase, the local region of $\{332\}\langle 113\rangle_\beta$ TB and $\alpha''$ phase.

### *3.4. The Nucleation and Structure Evolution of Martensite from Kinetic Calculations*

The nucleation of $\alpha''$ precipitation at $\{332\}\langle 113\rangle_\beta$ TB can also be further demonstrated within the framework of classical nucleation theory [45], by evaluating its nucleation driving energy and critical nucleation radius. Classical nucleation theory suggests that the nucleation of a new second phase is driven by volumetric energy reduction due to phase transformation, at the energy expense of creating new interphase interfaces. The driving energy ($\Delta G$) for the formation of the new second phase can be expressed as:

$$\Delta G = v\Delta G_v + \Sigma S\gamma, \tag{3}$$

where $v$ is volume of the new phase, $\Delta G_v$ is the free energy change per unit volume between the new and the parent phases, and $\Sigma S\gamma$ accounts for all interface energy contributions. In Equation (3), the strain energy can be incorporated into the interface energy owing to interface commensuration [46]. As the schematic shown in Figure 6a, the total driving energy for the nucleation scenario of $\alpha''$ at $\{332\}\langle 113\rangle_\beta$ TB can be expressed as:

$$\begin{aligned}\Delta G_1 &= v\Delta G_v^{(332)_\beta\to\alpha''} + (S_1+S_2)\gamma_{(110)_\beta//(001)_{\alpha''}} + S_1(\gamma_{(130)_{\alpha''}} - \gamma_{(332)_\beta}) \\ &= -\frac{1}{8}\pi r^3\Delta G_v^{(332)_\beta\to\alpha''} + \frac{5}{4}\pi r^2\gamma_{(110)_\beta//(001)_{\alpha''}} + \pi r^2(\gamma_{(130)_{\alpha''}} - \gamma_{(332)_\beta}),\end{aligned} \quad (4)$$

where $\Delta G_v^{(332)_\beta\to\alpha''}$ is the energy change due to the nucleation of $\alpha''$ at TB, which is evaluated from the energy difference between the instant structure firstly presenting $\alpha''$ phase at TB and the optimized $\{332\}\langle 113\rangle_\beta$ TB; and $S_1$ and $S_2$ are the areas of top/bottom and side surface of $\alpha''$ phase, respectively. Here, we suppose that the $\alpha''$ embryo takes a thin plate shape with the aspect ratio of $h = 1/8r$, where $h$ is the thickness and $r$ is the radius of the thin plate, since $\alpha''$ phase is generally observed in plate shape [47]. The thickness of $\alpha''$ plate is so small that we treat $\gamma_{(110)_\beta//(001)_{\alpha''}}$ as the side interface energy between $\alpha''$ plate and β matrix, based on the orientation relationship of $(110)_\beta//(001)_{\alpha''}$ determined in experiments [48,49]. The last term of Equation (4) accounts for the formation of $\{130\}\langle\bar{3}10\rangle_{\alpha''}$ TB from $\{332\}\langle 113\rangle_\beta$ TB. For the $\alpha''$ nucleation in β grain interior, its driving energy can be expressed as:

$$\Delta G_2 = v\Delta G_v^{\beta\to\alpha''} + S\gamma_{(110)_\beta//(001)_{\alpha''}} = -\frac{1}{8}\pi r^3\Delta G_v^{\beta\to\alpha''} + \frac{9}{4}\pi r^2\gamma_{(110)_\beta//(001)_{\alpha''}}. \quad (5)$$

Based on the energies listed in Tables 1 and 2, the driving energies of $\alpha''$ nucleation at $\{332\}\langle 113\rangle_\beta$ TB and in β grain interior were evaluated and are shown in Figure 6b. Note that the formation of $\alpha''$ phase at $\{332\}\langle 113\rangle_\beta$ TB is almost barrierless. However, there is an evident energy barrier of ~1900 eV for the formation of $\alpha''$ plate with the critical radius ($r_0$) of ~130 Å and the thickness of ~16 Å in β grain interior. This indicates that only the $\alpha''$ embryo with radius larger than $r_0$ can continue to grow up, otherwise it tends to disappear.

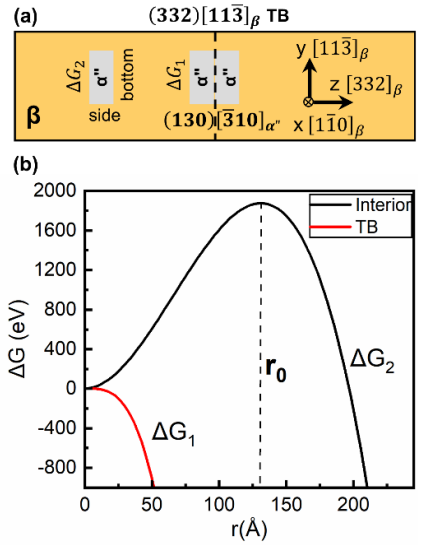


**Figure 6.** The kinetic behaviors of $\alpha''$ formation at the TB and in β grain interior. (**a**) The schematic of the different nucleation sites for $\alpha''$ phase at $\{332\}\langle 113\rangle_\beta$ TB and in β grain interior. (**b**) The driving energy curves associated with the formation of $\alpha''$ phase at $\{332\}\langle 113\rangle_\beta$ TB and in β grain interior.

Though the applied stress was not considered in our calculations, to some extent, this result can help us understand the reason why $\alpha''$ phase is easy to find when $\{332\}\langle 113\rangle_\beta$ TB exists in the experiments [13,15,50]. In the experimental study of Ti–Mo (wt.%) alloy, it is evidently shown that the volume fraction of $\alpha''$ phase from parent $\{332\}\langle 113\rangle_\beta$ TB is much higher than that of $\alpha''$ phase directly formed in β grain interior [13]. Based on our calculations, this higher volume fraction of $\alpha''$ phase from parent $\{332\}\langle 113\rangle_\beta$ TB may be well understood since the $\alpha''$ precipitation prefers to nucleate and grow at $\{332\}\langle 113\rangle_\beta$ TB rather than in β grain interior under the same external applied stress. It should be noted that the nucleation of martensite and its corresponding microstructure

evolution from $\{332\}\langle 113\rangle_\beta$ TB in our calculations are not universal but intrinsic, and the exact evolution process may be strongly dependent on the specific β-stabilizers. How the kind and concentration of β-stabilizers affect the inter-evolution between $\{332\}\langle 113\rangle_\beta$ TB and $\alpha''$ phase will be further investigated in our following studies.

## 4. Conclusions

In conclusion, our first-principles calculations show that pure β-Ti containing $\{332\}\langle 113\rangle_\beta$ TB has a tendency of transforming into $\alpha''$ phase. In this process, the martensite firstly nucleates at $\{332\}\langle 113\rangle_\beta$ TB, accompanying the transformation of $\{332\}\langle 113\rangle_\beta$ into $\{130\}\langle \bar{3}10\rangle_{\alpha''}$ TB, and it subsequently grows inwards toward the grain interiors. The $\{332\}\langle 113\rangle_\beta$ TB presents the characteristics of intermediate configuration between β and $\alpha''$ phases from the perspective of crystallography. The kinetic calculations show that $\alpha''$ phase prefers to nucleate at $\{332\}\langle 113\rangle_\beta$ TB and then grow inwards toward grain interiors barrierlessly, rather than in β grain interior. In this case, the critical driving energy of $\alpha''$ phase nucleation in β grain interior is estimated up to ~1900 eV, with the critical radius of ~130 Å. This study provides a detailed description of the martensite nucleation and its intrinsic microstructure evolution from $\{332\}\langle 113\rangle_\beta$ TB at atomic scale from a unique perspective, which may deepen our understanding on the precipitation of SIM $\alpha''$ phase within the $\{332\}\langle 113\rangle_\beta$ TB in β-Ti alloys. As a preliminary step, it also contributes to better understanding on the inter-evolution behaviors between $\{332\}\langle 113\rangle_\beta$ twinning and SIM $\alpha''$ and further study on the complicated process of TRIP/TWIP.

**Author Contributions:** Conceptualization, Q.-J.C. and S.-Y.M.; formal analysis, S.-Y.M.; funding acquisition, S.-Q.W.; investigation, Q.-J.C.; methodology, Q.-J.C. and S.-Y.M.; project administration, S.-Q.W.; supervision, S.-Q.W.; validation, Q.-J.C. and S.-Y.M.; writing—original draft, Q.-J.C.; writing—review and editing, S.-Y.M.

**Funding:** This work was funded by the National Key R&D Program of China, grant number 2016YFB0701302, and the CAS Frontier Science Research Project, grant numbers QYZDJ-SSW-JSC015 and QYZDY-SSW-JSC027.

**Acknowledgments:** This work was supported by the National Key R&D Program of China (No. 2016YFB0701302) and the CAS Frontier Science Research Project (No. QYZDJ-SSW-JSC015, QYZDY-SSW-JSC027). The authors thank the computational support from the Special Program for Applied Research on Super Computation of the NSFC-Guangdong Joint Fund (the second phase) under Grant No.U1501501. Most of the calculations in this study were done on the Tianhe-II high performance computer system in the National Supercomputer Center in Guangzhou, China.

**Conflicts of Interest:** The authors declare no conflicts of interest.

## References

1. Niinomi, M. Recent research and development in titanium alloys for biomedical applications and healthcare goods. *Sci. Technol. Adv. Mater.* **2003**, *4*, 445–454, doi:10.1016/j.stam.2003.09.002.
2. Banerjee, D.; Williams, J.C. Perspectives on Titanium Science and Technology. *Acta Mater.* **2013**, *61*, 844–879, doi:10.1016/j.actamat.2012.10.043.
3. Weiss, I.; Semiatin, S.L. Thermomechanical processing of beta titanium alloys—An overview. *Mater. Sci. Eng. A* **1998**, *243*, 46–65, doi:10.1016/s0921-5093(97)00783-1.
4. Williams, J.C.; Starke, E.A. Progress in structural materials for aerospace systems11The Golden Jubilee Issue—Selected topics in Materials Science and Engineering: Past, Present and Future, edited by S. Suresh. *Acta Mater.* **2003**, *51*, 5775–5799, doi:10.1016/j.actamat.2003.08.023.
5. Grosdidier, T.; Philippe, M.J. Deformation induced martensite and superelasticity in a β-metastable titanium alloy. *Mater. Sci. Eng. A* **2000**, *291*, 218–223, doi:10.1016/S0921-5093(00)00921-7.
6. Min, X.H.; Tsuzaki, K.; Emura, S.; Tsuchiya, K. Enhancement of uniform elongation in high strength Ti–Mo based alloys by combination of deformation modes. *Mater. Sci. Eng. A* **2011**, *528*, 4569–4578, doi:10.1016/j.msea.2011.02.071.
7. Marteleur, M.; Sun, F.; Gloriant, T.; Vermaut, P.; Jacques, P.J.; Prima, F. On the design of new β-metastable titanium alloys with improved work hardening rate thanks to simultaneous TRIP and TWIP effects. *Scr. Mater.* **2012**, *66*, 749–752, doi:10.1016/j.scriptamat.2012.01.049.

8. Ahmed, M.; Wexler, D.; Casillas, G.; Savvakin, D.G.; Pereloma, E.V. Strain rate dependence of deformation-induced transformation and twinning in a metastable titanium alloy. *Acta Mater.* **2016**, *104*, 190–200, doi:10.1016/j.actamat.2015.11.026.
9. Gao, J.; Huang, Y.; Guan, D.; Knowles, A.J.; Ma, L.; Dye, D.; Rainforth, W.M. Deformation mechanisms in a metastable beta titanium twinning induced plasticity alloy with high yield strength and high strain hardening rate. *Acta Mater.* **2018**, *152*, 301–314, doi:10.1016/j.actamat.2018.04.035.
10. Sun, F.; Zhang, J.Y.; Marteleur, M.; Brozek, C.; Rauch, E.F.; Veron, M.; Vermaut, P.; Jacques, P.J.; Prima, F. A new titanium alloy with a combination of high strength, high strain hardening and improved ductility. *Scripta Mater.* **2015**, *94*, 17–20, doi:10.1016/j.scriptamat.2014.09.005.
11. Ahmed, M.; Gazder, A.A.; Saleh, A.A.; Wexler, D.; Pereloma, E.V. Stress-Induced Twinning and Phase Transformations during the Compression of a Ti-10V-3Fe-3Al Alloy. *Metall. Mater. Trans. A* **2017**, *48*, 2791–2800, doi:10.1007/s11661-016-3675-4.
12. Zhang, J.Y.; Li, J.S.; Chen, Z.; Meng, Q.K.; Sun, F.; Shen, B.L. Microstructural evolution of a ductile metastable β titanium alloy with combined TRIP/TWIP effects. *J. Alloys Compd.* **2017**, *699*, 775–782, doi:10.1016/j.jallcom.2016.12.394.
13. Sun, F.; Zhang, J.Y.; Marteleur, M.; Gloriant, T.; Vermaut, P.; Laillé, D.; Castany, P.; Curfs, C.; Jacques, P.J.; Prima, F. Investigation of early stage deformation mechanisms in a metastable β titanium alloy showing combined twinning-induced plasticity and transformation-induced plasticity effects. *Acta Mater.* **2013**, *61*, 6406–6417, doi:10.1016/j.actamat.2013.07.019.
14. Castany, P.; Yang, Y.; Bertrand, E.; Gloriant, T. Reversion of a Parent {130} ⟨310⟩ $\alpha''$ Martensitic Twinning System at the Origin of {332} ⟨113⟩ β Twins Observed in Metastable β Titanium Alloys. *Phys. Rev. Lett.* **2016**, *117*, 245501, doi:10.1103/PhysRevLett.117.245501.
15. Lilensten, L.; Danard, Y.; Brozek, C.; Mantri, S.; Castany, P.; Gloriant, T.; Vermaut, P.; Sun, F.; Banerjee, R.; Prima, F. On the heterogeneous nature of deformation in a strain-transformable beta metastable Ti-V-Cr-Al alloy. *Acta Mater.* **2019**, *162*, 268–276, doi:10.1016/j.actamat.2018.10.003.
16. Ahmed, M.; Wexler, D.; Casillas, G.; Ivasishin, O.M.; Pereloma, E.V. The influence of beta phase stability on deformation mode and compressive mechanical properties of Ti-10V-3Fe-3Al alloy. *Acta Mater.* **2015**, *84*, 124–135, doi:10.1016/j.actamat.2014.10.043.
17. Chen, B.; Sun, W. Transitional structure of {332}<113>β twin boundary in a deformed metastable β-type Ti-Nb-based alloy, revealed by atomic resolution electron microscopy. *Scr. Mater.* **2018**, *150*, 115–119, doi:10.1016/j.scriptamat.2018.03.009.
18. Lai, M.J.; Tasan, C.C.; Raabe, D. On the mechanism of {332} twinning in metastable β titanium alloys. *Acta Mater.* **2016**, *111*, 173–186, doi:10.1016/j.actamat.2016.03.040.
19. Raabe, D.; Sander, B.; Friak, M.; Ma, D.; Neugebauer, J. Theory-guided bottom-up design of beta-titanium alloys as biomaterials based on first principles calculations: Theory and experiments. *Acta Mater.* **2007**, *55*, 4475–4487, doi:10.1016/j.actamat.2007.04.024.
20. Zhou, W.C.; Sahara, R.; Tsuchiya, K. First-principles study of the phase stability and elastic properties of Ti-X alloys (X = Mo, Nb, Al, Sn, Zr, Fe, Co, and O). *J. Alloys Compd.* **2017**, *727*, 579–595.
21. Kresse, G.; Hafner, J. Ab initio molecular-dynamics simulation of the liquid-metal--amorphous-semiconductor transition in germanium. *Phys. Rev. B* **1994**, *49*, 14251–14269, doi:10.1103/PhysRevB.49.14251.
22. Kresse, G.; Furthmüller, J. Efficient iterative schemes for ab initio total-energy calculations using a plane-wave basis set. *Phys. Rev. B* **1996**, *54*, 11169–11186, doi:10.1103/PhysRevB.54.11169.
23. Kresse, G.; Furthmuller, J. Efficiency of ab-initio total energy calculations for metals and semiconductors using a plane-wave basis set. *Comput. Mater. Sci.* **1996**, *6*, 15–50, doi:10.1016/0927-0256(96)00008-0.
24. Perdew, J.P.; Burke, K.; Ernzerhof, M. Generalized Gradient Approximation Made Simple. *Phys. Rev. Lett.* **1996**, *77*, 3865–3868, doi:10.1103/PhysRevLett.77.3865.
25. Kresse, G.; Joubert, D. From ultrasoft pseudopotentials to the projector augmented-wave method. *Phys. Rev. B* **1999**, *59*, 1758–1775.
26. Sheppard, D.; Xiao, P.; Chemelewski, W.; Johnson, D.D.; Henkelman, G. A generalized solid-state nudged elastic band method. *J. Chem. Phys.* **2012**, *136*, 074103, doi:10.1063/1.3684549.
27. Han, J.; Vitek, V.; Srolovitz, D.J. The grain-boundary structural unit model redux. *Acta Mater.* **2017**, *133*, 186–199, doi:10.1016/j.actamat.2017.05.002.

28. Sutton, A.P.; Vitek, V. On the structure of tilt grain boundaries in cubic metals I. Symmetrical tilt boundaries. *Philos. Trans. R. Soc. A-Math. Phys. Eng.* **1983**, *309*, 1–36, doi:10.1098/rsta.1983.0020.
29. Tschopp, M.A.; Solanki, K.N.; Gao, F.; Sun, X.; Khaleel, M.A.; Horstemeyer, M.F. Probing grain boundary sink strength at the nanoscale: Energetics and length scales of vacancy and interstitial absorption by grain boundaries in alpha-Fe. *Phys. Rev. B* **2012**, *85*, 064108, doi:10.1103/PhysRevB.85.064108.
30. Bhattacharya, S.K.; Tanaka, S.; Shiihara, Y.; Kohyama, M. Ab initio study of symmetrical tilt grain boundaries in bcc Fe: Structural units, magnetic moments, interfacial bonding, local energy and local stress. *J. Phys. Condens. Matter* **2013**, *25*, 135004.
31. Hahn, E.N.; Fensin, S.J.; Germann, T.C.; Meyers, M.A. Symmetric tilt boundaries in body-centered cubic tantalum. *Scr. Mater.* **2016**, *116*, 108–111.
32. Monkhorst, H.J.; Pack, J.D. Special points for Brillouin-zone integrations. *Phys. Rev. B* **1976**, *13*, 5188–5192, doi:10.1103/PhysRevB.13.5188.
33. Pack, J.D.; Monkhorst, H.J. "Special points for Brillouin-zone integrations"—A reply. *Phys. Rev. B* **1977**, *16*, 1748–1749, doi:10.1103/PhysRevB.16.1748.
34. Joost, W.J.; Ankem, S.; Kuklja, M.M. Interaction between oxygen interstitials and deformation twins in alpha-titanium. *Acta Mater.* **2016**, *105*, 44–51.
35. Kumar, A.; Wang, J.; Tome, C.N. First-principles study of energy and atomic solubility of twinning-associated boundaries in hexagonal metals. *Acta Mater.* **2015**, *85*, 144–154, doi:10.1016/j.actamat.2014.11.015.
36. Mei, Z.-G.; Shang, S.-L.; Wang, Y.; Liu, Z.-K. Density-functional study of the thermodynamic properties and the pressure--temperature phase diagram of Ti. *Phys. Rev. B* **2009**, *80*, 104116, doi:10.1103/PhysRevB.80.104116.
37. Persson, K.; Ekman, M.; Ozolins, V. Phonon instabilities in bcc Sc, Ti, La, and Hf. *Phys. Rev. B* **2000**, *61*, 11221–11224, doi:10.1103/PhysRevB.61.11221.
38. Grimvall, G.; Magyari-Kope, B.; Ozolins, V.; Persson, K.A. Lattice instabilities in metallic elements. *Rev. Mod. Phys.* **2012**, *84*, 945–986, doi:10.1103/RevModPhys.84.945.
39. Vohra, Y.K.; Spencer, P.T. Novel gamma-phase of titanium metal at megabar pressures. *Phys. Rev. Lett.* **2001**, *86*, 3068–3071, doi:10.1103/PhysRevLett.86.3068.
40. Zimmermann, F.; Humbert, M. Determination of the habit plane characteristics in the β–α′ phase transformation induced by stress in Ti–5Al–2Sn–4Zr–4Mo–2Cr–1Fe. *Acta Mater.* **2002**, *50*, 1735–1740, doi:10.1016/S1359-6454(02)00022-8.
41. Li, C.-X.; Luo, H.-B.; Hu, Q.-M.; Yang, R.; Yin, F.-X.; Umezawa, O.; Vitos, L. Lattice parameters and relative stability of α″ phase in binary titanium alloys from first-principles calculations. *Solid State Commun.* **2013**, *159*, 70–75, doi:10.1016/j.ssc.2013.01.026.
42. Kim, H.Y.; Ikehara, Y.; Kim, J.I.; Hosoda, H.; Miyazaki, S. Martensitic transformation, shape memory effect and superelasticity of Ti–Nb binary alloys. *Acta Mater.* **2006**, *54*, 2419–2429, doi:10.1016/j.actamat.2006.01.019.
43. Bertrand, E.; Castany, P.; Yang, Y.; Menou, E.; Gloriant, T. Deformation twinning in the full-α″ martensitic Ti–25Ta–20Nb shape memory alloy. *Acta Mater.* **2016**, *105*, 94–103, doi:10.1016/j.actamat.2015.12.001.
44. Mantri, S.A.; Sun, F.; Choudhuri, D.; Alam, T.; Gwalani, B.; Prima, F.; Banerjee, R. Deformation Induced Hierarchical Twinning Coupled with Omega Transformation in a Metastable β-Ti Alloy. *Sci. Rep.* **2019**, *9*, 1334, doi:10.1038/s41598-018-37865-0.
45. Drossinos, Y.; Kevrekidis, P.G. Classical nucleation theory revisited. *Phys. Rev. E* **2003**, *67*, 026127, doi:10.1103/PhysRevE.67.026127.
46. Li, D.; Wan, W.; Zhu, L.; Jiang, Y.; Shao, S.; Yang, G.; Liu, H.; Yi, D.; Cao, S.; Hu, Q. Experimental and DFT characterization of interphase boundaries in titanium and the implications for ω-assisted α phase precipitation. *Acta Mater.* **2018**, *151*, 406–415, doi:10.1016/j.actamat.2018.03.056.
47. Yin, J.O.; Chen, G.; Zhao, S.Y.; Ge, Y.; Li, Z.F.; Yang, P.J.; Han, W.Z.; Wang, J.; Tang, H.P.; Cao, P. Microstructural characterization and properties of Ti-28Ta at.% powders produced by plasma rotating electrode process. *J. Alloys Compd.* **2017**, *713*, 222–228, doi:10.1016/j.jallcom.2017.04.195.
48. Frutos, E.; Karlík, M.; Jiménez, J.A.; Langhansová, H.; Lieskovská, J.; Polcar, T. Development of new β/α″-Ti-Nb-Zr biocompatible coating with low Young's modulus and high toughness for medical applications. *Mater. Des.* **2018**, *142*, 44–55, doi:10.1016/j.matdes.2018.01.014.

49. Yao, T.; Du, K.; Wang, H.; Huang, Z.; Li, C.; Li, L.; Hao, Y.; Yang, R.; Ye, H. In situ scanning and transmission electron microscopy investigation on plastic deformation in a metastable β titanium alloy. *Acta Mater.* **2017**, *133*, 21–29, doi:10.1016/j.actamat.2017.05.018.
50. Furuhara, T.; Nakamori, H.; Maki, T. Crystallography of α Phase Precipitated on Dislocations and Deformation Twin Boundaries in a β Titanium Alloy. *Mater. Trans. JIM* **1992**, *33*, 585–595, doi:10.2320/matertrans1989.33.585.